

See discussions, stats, and author profiles for this publication at: <https://www.researchgate.net/publication/299443393>

# Stacking fault energies in austenitic stainless steels

Article in *Acta Materialia* · June 2016

DOI: 10.1016/j.actamat.2016.03.042

CITATIONS

211

READS

5,575

8 authors, including:



**Jun Lu**

Linköping University

248 PUBLICATIONS 30,177 CITATIONS

SEE PROFILE



**Lars Hultman**

Linköping University

882 PUBLICATIONS 68,478 CITATIONS

SEE PROFILE



**Erik Holmström**

Sandvik Group

89 PUBLICATIONS 2,973 CITATIONS

SEE PROFILE



**Mikael Grehk**

Karlstads Universitet

70 PUBLICATIONS 1,526 CITATIONS

SEE PROFILE

# Stacking Fault Energies in austenitic stainless steels

Jun Lu,<sup>1</sup> Lars Hultman,<sup>1</sup> Erik Holmström,<sup>2</sup> Karin H. Antonsson,<sup>3</sup>  
Mikael Grehk,<sup>3</sup> Wei Li,<sup>4</sup> Levente Vitos,<sup>4</sup> and Ardeshir Golpayegani<sup>3</sup>

<sup>1</sup>*Thin Film Physics Division, Dept. of Physics, Chemistry and Biology (IFM),  
Linköping University, SE-581 83 Linköping Sweden*

<sup>2</sup>*Sandvik Coromant R&D, SE-126 80 Stockholm Sweden\**

<sup>3</sup>*R&D Center, Sandvik Materials Technology, Sandviken SE-81181, Sweden*

<sup>4</sup>*Applied Materials Physics, Department of Materials Science and Engineering,  
Royal Institute of Technology, Stockholm SE-100 44, Sweden*

(Dated: January 19, 2016)

We measure the stacking fault energy of a set of 20 at% Cr-austenitic stainless steels by means of transmission electron microscopy using the weak beam dark field imaging technique and the isolated dislocations method. The measurements are analyzed together with first principles calculations. The results show that experiment and theory agree very well for the investigated concentration range of Mn (0-8%) and Ni (11-30%). The calculations show that simultaneous relaxation of atomic and spin degrees of freedom is important in order to find the global energy minimum for these materials. Our results clearly show the great potential of the weak beam dark field technique to obtain accurate measurements of the stacking fault energy of austenitic steels and that the reliable predictability of first principles calculations can be used to design new steels with optimized mechanical properties.

## I. INTRODUCTION

The stacking-fault energy (SFE) is a composition and temperature-dependent characteristic of crystalline materials and plays an important role for the austenitic steel deformation.<sup>1,2</sup> Plasticity of austenitic stainless steels is generally achieved by a combination of deformation mechanisms and twinning strain itself may contribute a relatively small amount to the elongation. Their primary influence seem to be that they enhance the work-hardening rate by subdividing the grains into twinned and untwinned regions and thereby delaying local necking.<sup>3</sup>

Although larger deformation modes, like e.g. dislocation glide, may be present, the importance of the twinning contribution depends on the SFE. Low SFE (<20 mJ/m<sup>2</sup>) favors the phase transformation from austenitic phase to martensitic phase ( $\epsilon$ - or  $\alpha'$ -martensitic transformations) and leads to phase transformation induced plasticity (TRIP); Middle SFE (20-45 mJ/m<sup>2</sup>) yields deformation through twinning mechanisms, leading to twinning induced plasticity (TWIP). In the high SFE case (>45 mJ/m<sup>2</sup>), dislocations are rarely dissociated, thus, the deformation process is controlled mainly by dislocation glide.<sup>4</sup>

By adjusting the SFE to a proper value, a suitable austenitic stainless steel with desired mechanical properties can be designed and produced. The SFE of stainless steel is strongly dependent on its composition. To achieve TRIP or TWIP, a low value of the SFE is desired and possible to achieve by tuning the chemical composition of the designed stainless steel. However, the details of the composition influence from alloying elements on

the SFE is complex and need to be investigated closely in each case in order to be fully understood. For instance, Ni and Cr raise the SFE in Fe-Mn alloys but have the inverse effect for carbon steels.<sup>5</sup> The correlation between the SFE and composition can be experimentally investigated by X-ray diffraction<sup>6</sup> or transmission electron microscopy (TEM),<sup>7-9</sup> or estimated by empirical relationships.<sup>10</sup> The outcome from the experimental methods relies on the resolution, sample preparation, and assumptions made in the evaluation process. Other factors are the micro-structural properties of the alloy under investigation in terms of grain size, number of inclusion residual stresses and purity and in particular the concentration levels of interstitial atoms such as N and C. The latter property depends on quality of melting and casting and the following thermomechanical treatment of the alloy. Without proper control of how the samples are manufactured, the results from experiments have a potential of high levels of error and sometimes result in contradictory data compared to similar studies. The drawback of empirical methods is its application limitation due to the limited available data. Furthermore, the complicated interactions of different elements is difficult to represent by a simple empirical formula.

To explore the influence of different elements on the SFE and the mutual correlations between the elements, theoretical calculations is an effective method. Computational thermodynamics has recently been used<sup>11-15</sup> and several groups have investigated SFE via quantum mechanical first-principles calculations for steels.<sup>16,17</sup> The advantage with such calculations is the ease by which the theory provides fundamental understanding of the effects that the complex relationships between the different elements have on the SFE. The calculations can also span a whole concentration space to provide insights on general trends. In order to perform calculations over large concentration spaces it is necessary to make bal-

---

\*Electronic address: erik.holmstrom@sandvik.com

anced approximations so that the computational effort is minimized. To verify the approximations that are used in the calculations, SFE values from selected reference alloys should be measured experimentally.

SFE for steels has been obtained experimentally previously by TEM<sup>7-9,14,18,19</sup>. However, a quantitative comparison between calculations and measured SFE has traditionally been hampered by the large uncertainties in both the measured values and in the approximations used in the calculations. The aim of this work is to measure the SFE of a set of high-purity stainless steels on the most quantitative level possible via TEM and subsequently compare the experimental data with state-of-the-art theoretical first principles simulations.

## II. EXPERIMENT

### A. Experimental measurement of SFE by TEM

Transmission electron microscopy (TEM) can be used to determine SFE in different ways; 1) high-resolution TEM (HRTEM) where the width of a stacking fault is observed directly in cross-section;<sup>20</sup> 2) the extended dislocation node method;<sup>7</sup> and 3) the isolated dislocation approach.<sup>21-23</sup> In general, the HRTEM method is the most direct since it measures a visible quantity, but it has drawbacks. It needs a very thin sample region, which means a very limited area is available for this kind of characterization. Because of the very thin specimen, the surface effect on the SFE cannot be eliminated. It should be noted that the HRTEM method may be the sole way for some materials with very high SFE because of the high point resolution.<sup>20</sup> The extended node method to measure SFE by TEM was first suggested by Whelan.<sup>24</sup> This technique does not have resolution problems to measure the radius of curvature (R) of extended nodes. However, it is difficult to determine R as nodes are rarely symmetrical or uniform in size. In addition, there are no simple relationships between the geometrical parameters of the node and the corresponding SFE, resulting in a large scatter of measured SFE values.<sup>7</sup> The third method, the isolated dislocation method is a promising technique since SFE of high accuracy ( $16 \pm 2$  mJ/m<sup>2</sup>) has been shown possible to measure for Fe-Mn-Al-Si austenitic twinning-induced plasticity steels.<sup>7</sup> Due to the demonstrated accuracy of the isolated dislocation technique, this approach was chosen in the present study.

#### 1. Isolated dislocation method

According to Heidenreich & Shockley's suggestion, a perfect dislocation in a face-centered cubic lattice can dissociate into two partial dislocations.<sup>25</sup> The two partial dislocations repel each other and leave a stacking fault between them. The distance  $d$  (dissociation width) between the two partial dislocations is determined by the

attractive force exerted by the stacking fault and the repulsive interaction between the partial-dislocation strain fields. Thus, SFE, here denoted  $\gamma$  can be calculated based on anisotropic elasticity theory. The equation below is in the general case an approximation to anisotropic elasticity theory that is based on isotropic theory. In our case of  $\{111\}$  glide planes and dislocations along  $[110]$ , the equation is exact<sup>26</sup> and

$$\gamma = \frac{\mu b_p^2}{8\pi d} \left( \frac{2-\nu}{1-\nu} \right) \left( 1 - \frac{2\nu \cos 2\alpha}{2-\nu} \right) \quad (1)$$

where  $\mu$  is the effective shear modulus in the  $(111)$  fault plane,  $\nu$  is the effective Poisson ratio and  $\alpha$  is the angle between the total Burgers vector and the dislocation line.  $b_p$  is the magnitude of the partial Burgers vector, which is approximately 0.148 nm for the lattice parameters of the materials in this study and  $d$  is the separation of the partials, which is to be measured. The effective shear modulus  $\mu$  and Poisson ratio  $\nu$  were calculated for each sample according to the following equations:

$$\mu = \left( C_{44} \frac{(C_{11} - C_{12})}{2} \right)^{0.5} \quad (2)$$

$$\frac{1}{1-\nu} = \frac{1}{3\mu} (C + C_{12}) \left[ \frac{C_{44}(C - C_{12})}{C_{11}(C + C_{12} + 2C_{44})} \right]^{0.5} \left( 1 + 2 \frac{C_{11}}{C} \right) \quad (3)$$

where

$$C = \left[ \frac{1}{2} C_{11}(C_{11} + C_{12} + 2C_{44}) \right]^{0.5}. \quad (4)$$

We used experimental elastic stiffness constants from ref. [27] where alloys with very similar concentrations were measured. In the cases where the exact alloy concentrations could not be found, we used data from the closest available alloy. Since the values of the elastic constants do not change much when the alloy concentrations are altered by a few percent this error is well within the measurement uncertainty of the elastic constant themselves. In the case of the samples that contain Mn we have not been able to obtain elastic constants so we have used the same values as for the samples without Mn.

Since the value of  $d$  is in the nanometer range, the weak beam image technique is available to determine the separated partials at the condition of the effective excitation error  $s > 0.2$  nm<sup>-1</sup>.<sup>22</sup>

The relationships between the perfect dislocations, the relative partial dislocations and the corresponding reflections are demonstrated by the Thompson tetrahedron<sup>28</sup> as shown in figure 1. It can be seen that a perfect dislocation can be dissociated into two partial dislocations

$$\frac{a}{2}[\bar{1}10] \leftrightarrow \frac{a}{6}[\bar{1}2\bar{1}] + \frac{a}{6}[\bar{2}11]. \quad (5)$$

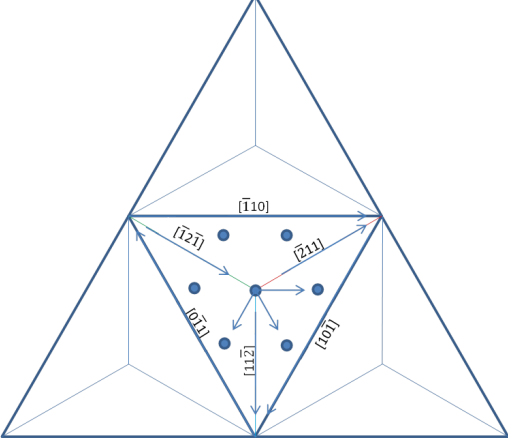


FIG. 1: Thompson tetrahedron showing the relationship between the perfect and partial dislocations.

Moreover, the Burgers vectors  $[1\bar{1}0]$ ,  $[1\bar{2}1]$  and  $[2\bar{1}\bar{1}]$  are in the  $(111)$  plane. In addition, in the same plane, there are another two perfect dislocations  $[10\bar{1}]$  and  $[0\bar{1}1]$ , which can be dissociated into  $[11\bar{2}]$ ,  $[2\bar{1}\bar{1}]$  and  $[1\bar{2}1]$ ,  $[1\bar{1}2]$ , respectively. To determine the SFE, the separation of two partial dislocations ( $d$ ) and the angle between the total Burgers vector and the perfect dislocation line  $\alpha$  have to be measured.

To ensure that the dislocations are lying in a perpendicular  $(111)$  plane, the specimen is needed to be aligned with the  $111$  zone axis parallel to the electron beam. Then the reflections  $\bar{2}20$ ,  $20\bar{2}$  and  $0\bar{2}2$  are excited, which can be used to show partials  $\frac{a}{6}[\bar{1}2\bar{1}]$ ,  $\frac{a}{6}[\bar{2}1\bar{1}]$  etc. For polycrystalline samples, some  $\bar{2}20$  reflections in other  $\{111\}$  planes such as the  $(11\bar{1})$  zone axis may also be present in the partials but such  $\bar{2}20$  reflections have been excluded in our experiments since all the dislocations we observed are within the same grain (like a single crystal specimen), which has been aligned in the  $111$  zone axis. Thus, we can conclude that all the dislocations we found are in the  $(111)$  plane.

## 2. The weak beam dark field technique (WBDF)

To obtain  $\alpha$  easily, the sample in the  $111$  zone axis (see figure 2a) is desired for the formation of weak beam images. To achieve the  $\bar{g}(3\bar{g})$  weak beam condition, the specimen should be tilted a few degrees along the  $\bar{2}20$  axis from the  $111$  zone axis direction to form a one line diffraction condition, followed by tilting the sample perpendicular to the  $\bar{2}20$  direction to form a two beam condition, so that only the  $000$  and  $\bar{2}20$  beams are strongly excited (see figure 2b)). A centered weak beam is obtained by centering the  $\bar{2}20$  beam. Thus, the  $\bar{g}(3\bar{g})$  weak beam condition is gained (see figure 2c)) as applied in

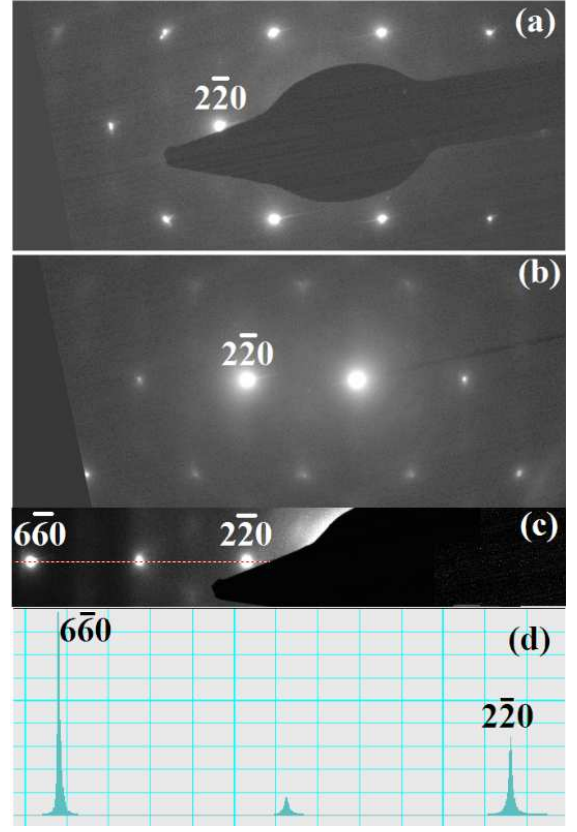


FIG. 2: (a) a SAED pattern along  $111$  zone axis, (b) one line diffraction pattern along  $\bar{2}20$  direction, (c)  $\bar{g}(3\bar{g})$  condition obtained by centering  $\bar{2}20$  beam, (d) intensity profile of the reflections in (c).

this study. In this case, only the  $6\bar{6}0$  and  $000$  beams are strongly excited, while the  $\bar{2}20$  beam is relatively weak compared to the  $6\bar{6}0$  reflection (see the intensity profile in figure 2d)). The weak beam dark field image is created by selecting the  $\bar{2}20$  reflection with the objective lens aperture.

## B. Experimental details

### 1. Sample preparation

The six alloys were melted and cast as 170-270 kg ingots in a vacuum induction melting furnace (VIM) and then quenched in water. The chemical analysis of the heats can be found in table (I). Forging of the as-cast ingots were done to dimension  $136 \times 56$  mm. Furnace temperature at forging was  $1250^\circ\text{C}$  for alloys without Mn and  $1200^\circ\text{C}$  for Mn-containing alloys. After forging, the material was quench-annealed; with a furnace temperature of  $1200^\circ\text{C}$ , a holding time of 30 minutes and then water quenching. Hot rolling was done to reach the final thickness of 15 mm; the furnace temperature during hot rolling was  $1210^\circ\text{C}$  for alloys without Mn and

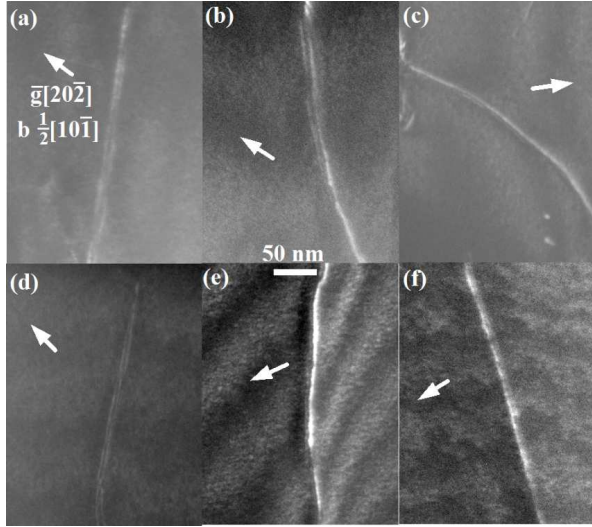


FIG. 3: WBDF images of a dissociated dislocation in the samples (a): #2, (b): #1, (c): #3, (d): #4, (e): #5, and (f): #6. The reflection used to form the image and total Burgers vectors are marked as  $\vec{g}[202]$  and  $\vec{b}_{\frac{1}{2}}[101]$  respectively and are shown by white arrows.

1180°C for Mn-containing alloys. After the final rolling pass the material was quench-annealed again for 20 minutes at 1210°C for alloys without Mn and 1180°C for Mn-containing alloys before quenching in water. The nitrogen level was <0.008wt%, carbon <0.009wt% and the total amount of trace elements was below 0.15wt%. For a complete listing of sample compositions, see table (I).

The TEM specimens were prepared by mechanically polishing a disc with a size of 3 mm in diameter down to 0.1 mm followed by electrochemical polishing to electron transparency. A conventional twin-jet method with a 10% hydrochloric acid was used for the electrochemical polishing at -15°C. Six samples with different SFE and varied Mn and Ni concentrations were selected for the measurement. The TEM characterization was carried out by using a FEI Tecnai UT electron microscope operated at 200 kV with 0.19 nm point resolution. The  $\vec{g}(3\vec{g})$  WBDF technique was utilized to achieve the large excitation error ( $s_g$ ).

In general, the SFE is influenced by many parameters such as grain size, temperature, and chemical composition. Temperature may influence the SFE in Fe alloys that are close to a phase transition<sup>29</sup> and for austenitic steels with compositions far from the phase transition, the SFE is believed to be almost linearly proportional to temperature under normal conditions.<sup>12</sup> In this work, only the effect of chemical composition is investigated and so that all measurements and calculations are carried out at room temperature. The grain size also plays a role on the SFE for Fe-Mn alloys and has been shown to be significant when the grain size is less than 35  $\mu\text{m}$ .<sup>30</sup>

However, so far there is no clear conclusion on the effect of grain size on the SFE for stainless steels. The grain size effect was thus not considered in this work.

Suzuki segregation<sup>31</sup> is the result of impurity concentration build-up around stacking faults and other crystal imperfections and may influence the SFE as well. The effect is usually found in heat treated samples where the temperature has been maintained high enough for the impurities so diffuse to the imperfection. Another possibility is that a dislocation may sweep the crystal and pick up impurities that then diffuse along with the imperfection. If Suzuki segregation is present, the local alloy concentration as the imperfection will differ from the average over the whole sample, effectively changing the properties of the imperfection such as the stacking fault energy. However, the temperatures we use and subsequent water quenching of the samples will minimize the probability of impurity segregation to the stacking faults.

## C. Computational Methods

### 1. First-principles method

The most common stacking fault in an fcc crystal, the so-called intrinsic stacking fault, may be viewed as a missing (111) layer from an otherwise perfect lattice. According to the pioneering work by Ishida<sup>32</sup>, this SFE, to a good approximation, is proportional to the Gibbs energy difference between the hexagonal close packed (hcp) and face centered cubic (fcc) phases.

An extension of the Isida approximation is the axial interaction model<sup>33</sup> where interactions between layers up to the third nearest neighbors are taken into account. In this approach, the SFE can be obtained from the free energies of the hcp, double hcp (dhcp) and fcc lattices as

$$\gamma = \Delta F \simeq [F_{hcp} + 2F_{dhcp} - 3F_{fcc}] / A_{2D}. \quad (6)$$

if the free energies are expressed as energy per atom. Here, the excess free energy  $\Delta F$  per unit interface area ( $A_{2D}$ ) defines the fault energy  $\gamma$ .

We used the exact muffin-tin orbitals (EMTO) method<sup>34</sup> to compute the terms in eq. (6) for a set of  $\text{Fe}_{100-n-c}\text{Cr}_c\text{Ni}_n$  alloys. This method, in combination with the coherent potential approximation (CPA)<sup>35</sup>, is suitable for describing the simultaneous presence of the chemical and magnetic disorder in Fe-based random alloys.<sup>36,37</sup> For pure Fe, the magnetic free energy vanishes in the hcp phase ( $\epsilon\text{-Fe}$ ),<sup>38</sup> indicating that the local moments disappear. This means that we must account for the possibility of zero local moments in the calculations of our alloy compositions.

In the present study the paramagnetic phase of the  $\text{Fe}_{100-n-c}\text{Cr}_c\text{Ni}_n$  alloy was modeled by the quasiternary  $(\text{Fe}_{1/2}^{\uparrow}\text{Fe}_{1/2}^{\downarrow})_{100-c-n} (\text{Cr}_{1/2}^{\uparrow}\text{Cr}_{1/2}^{\downarrow})_c (\text{Ni}_{1/2}^{\uparrow}\text{Ni}_{1/2}^{\downarrow})_n$  alloy with randomly distributed magnetic moments oriented



Sample	#1	#2	#3	#4	#5	#6
Fe	68.9	65.9	60.1	50.2	57.8	52.3
Ni	10.8	13.6	19.6	29.4	13.3	19.4
Cr	20.2	20.2	20.2	20.3	20.5	20.1
Mn	0.041	0.052	0.031	0.031	8.20	8.10
C	0.026	0.026	0.030	0.026	0.039	0.030
Si	0.037	0.055	0.037	0.037	0.055	0.037
S	0.008	0.010	0.008	0.008	0.010	0.010
N	0.026	0.026	0.022	0.022	0.029	0.026
Al	0.008	< 0.006	0.024	0.026	< 0.006	0.008
O	0.016	0.039	0.008	0.008	0.021	0.017

TABLE I: Chemical analysis of sample compositions of the samples in this study. All compositions are given in atom %.

up( $\uparrow$ ) and down( $\downarrow$ ). This approximation accurately describes the effect of loss of the net magnetic moment above the transition temperature<sup>33,39,40</sup> as well as the possible loss of local moments in the hcp phase.

The temperature dependent magnetic moment  $\mu(T)$ , representing the set of local magnetic moments, can be determined from the minimum of the free energy  $F(T, \mu) = E(T, \mu) - T[S_{mag}(\mu) + S_{el}(T)]$  calculated at the theoretical equilibrium volume. The electronic energy  $E(T, \mu)$  was obtained from spin constrained calculations. The electronic contribution to the entropy was neglected. The magnetic entropy was estimated using the mean-field expression  $S_{mag}(\mu) = k_B \log(1 + \mu)$  ( $k_B$  is the Boltzmann constant) valid for completely disordered localized moments, as described in ref. [41]. The explicit phonon contribution to  $\Delta F$  was neglected, which was estimated to introduce an error  $\sim 2$  mJ/m<sup>2</sup> in  $\gamma$ <sup>42,43</sup>. Since the calculations are performed at a fixed temperature, no volume expansion effects are included in the theoretical results and hence the anharmonic part of the phonon contribution to the SFE was neglected. The number of k-points was carefully chosen to minimize the convergence error for each crystal structure below  $1\mu\text{Ry}$  per atom. The Perdew-Burke-Ernzerhof<sup>44</sup> (PBE) parameterization of the exchange correlation functional was used. The change in energy of the deep electronic core levels due to the chemical bonding was not taken into account. Some results from this frozen core approximation were checked against calculations where the core levels were allowed to interact with the valence electrons and the change in calculated energy differences was negligible. In the present work, the first principles calculations are performed for Fe-Cr-Ni-Mn alloys containing 0 at% and 8 at% Mn and a fixed amount of 20 at% Cr, the Ni amount is varied between 8 at% and 30 at%.

In our experimental samples we have both C and N present in low, but detectable, amounts. It has been shown that small amounts of C and N may have an effect on the SFE and several empirical equations have been reported.<sup>45-47</sup> The strength of the effect is however not agreed upon and different studies give very different estimates. In our case, the levels of C and N are very small and fall outside of the composition range where the empirical equation of reference [45] is valid. However, the

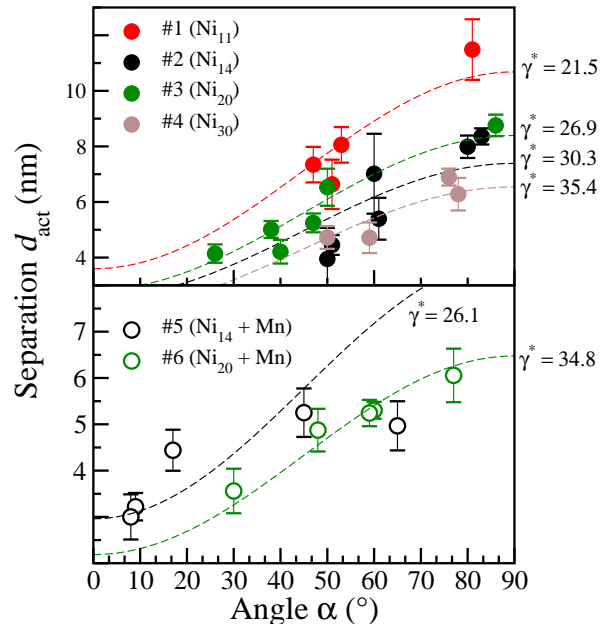


FIG. 4: The actual partial dislocation spacing as a function of total dislocation character angle for the samples with different SFE. The dashed lines correspond to the best fitted eq. (1) for each sample and the values on the right side represent the  $\gamma$  in units of mJ/m<sup>2</sup> that was the result of the best fit.

composition range of the empirical equation given in reference [47] includes our C and N levels. In that reference, the suggested influence of carbon on the SFE is given as  $26\text{wx}\%C$ , which in our alloys amounts to a maximum of 0.23 mJ/m<sup>2</sup> for sample #5 where the impurity concentration of C is the largest. We hence assume that the effects of C and N can be neglected for our samples and do not include C and N in the DFT calculations.

### III. RESULTS AND DISCUSSION

#### A. WBDF measurements

Figures 3(a-f) are the WBDF images of samples #2-#6 (see also table II), illustrating partial dislocations for

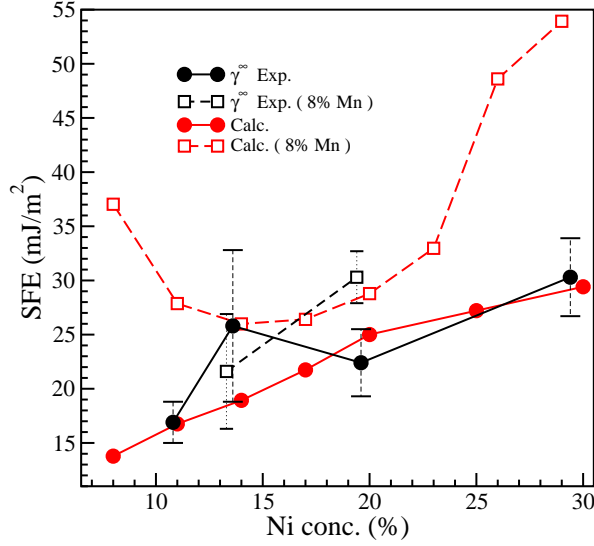


FIG. 5: The calculated and measured ideal stacking fault energies of FeNiCr alloys. Legends with the notation (Mn) indicate samples that contain 8% Mn.

each sample. All the specimens were tilted with the incident beam direction near  $[111]$  to simplify the partial separation measurements and Burgers vector analysis. The WBDF image was formed with the centered  $20\bar{2}$  reflection. In this case, the Burgers vector of perfect dislocation is parallel to the reflection, leading to both partial dislocations visible, otherwise only one partial dislocation can be observed. Thus, the Burgers vector of the perfect dislocation is  $\frac{1}{2}[10\bar{1}]$ , as shown in figure 3. The angle  $\alpha$  between the total Burgers vector and the perfect dislocation line can be measured. The separation between the two partial dislocations are measured from the dislocation in the images. We took care that the studied dislocations were separated by at least 200 nm from each other or other defects in order to avoid stress field effects. The actual position of the dislocation in WBDF images is not exactly corresponding to the position of the dislocation cores. It depends on the value of the excitation error, the depth of the dislocation within the foil and the sample thickness. Therefore, the measured dissociation width  $d_{obs}$  must be corrected by the following weak-beam formula,<sup>48,49</sup>

$$d_{act} = \sqrt{(d_{obs}^2 - \frac{4}{ab})} + \frac{b-a}{ab} \quad (7)$$

$$a = -\frac{2\pi s_g}{g(b_{p1} + \frac{b_{p1e}}{2(1-\nu)})} \quad (8)$$

$$b = -\frac{2\pi s_g}{g(b_{p2} + \frac{b_{p2e}}{2(1-\nu)})} \quad (9)$$

where  $\nu$  is the Poisson ratio,  $b_{p1}$ ,  $b_{p2}$  and  $b_{p1e}$ ,  $b_{p2e}$  are the Burgers vectors of the partial dislocations and their edge

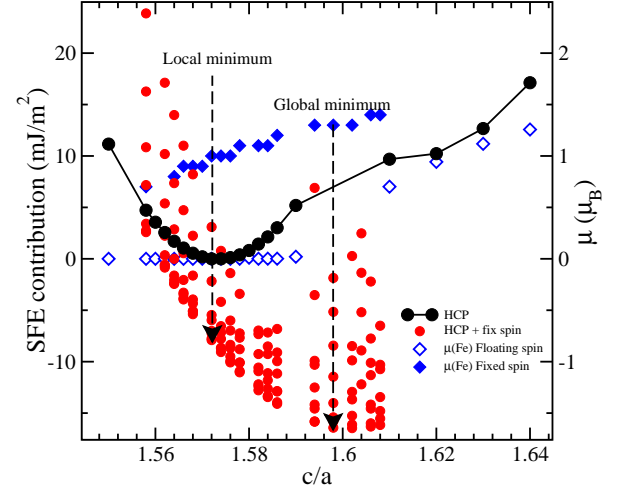


FIG. 6: The contribution to the stacking fault energy from the intermediate spin state of the  $\text{Fe}_{66}\text{Ni}_{14}\text{Cr}_{20}$  alloy in the hcp structure.

components. Figure 4 illustrates the actual partial dislocation spacing as a function of total dislocation character angle. To reduce the error in the measurement, several images containing a couple of isolated long dislocations were acquired for each sample. Each point in the figure represents a measurement of eight partial dislocation spacings along one unique partial dislocation pair.

To get an average value, eq. (1) was fitted to the set of data points for each sample by means of an ordinary, non weighted, least squares procedure. The resulting angle-spacing relations are shown in figure 4 as dashed lines. We estimate the error in position determination to be less than 1 nm and this error is included in the data presented in table II. Also included in the error bars is the scatter of the distance measurements along each dislocation pair.

We have assumed that the coherency strain between the fault and the matrix in our set of samples is similar to the measured strain of an intrinsic stacking fault of an 18.5w%Cr - 10.05w%Ni steel from reference [50,51]. There it was found that the strain is about 2% around the intrinsic stacking fault, which can be modeled as a strain induced contribution to the stacking fault by the following equation:<sup>52</sup>

$$\gamma^\infty = \gamma^* - \frac{s\mu\epsilon^2}{2(1-\nu)} \quad (10)$$

where  $\gamma^\infty$  is the ideal stacking fault energy,  $\gamma^*$  is the measured effective stacking fault energy,  $s$  is the interplanar spacing, and  $\epsilon$  is the strain normal to the fault plane. The used values depend on the interplanar spacings, Poissons ratio, and the shear modulus of the particular alloy and we use the same values for these parameters as in the evaluations of the stacking fault measurements.

## B. Stacking fault energies

### 1. $FeNi_{(8-40)}Cr_{20}$ samples

In figure 5 we show a comparison between the calculated and measured SFE energies. We can see that increasing nickel content raises the SFE from about 14 mJ/m<sup>2</sup> at 8% Ni to close to 30 mJ/m<sup>2</sup> at 30% Ni, which is consistent with an expected positive effect of Ni content on SFE. However, the Ni influence is complicated by the discrepancy between the calculation and measurement of the 14% Ni sample where the calculation gives about 6.6 mJ/m<sup>2</sup> lower value compared to the experiment. When the Ni composition is increased from 14 at% to 20 at%, the measured SFE value decreases slightly. On the whole, the measured and calculated points agree very well over the whole concentration range. If we compare our calculated value with previous results from Ref. 17 (c.f table II) we can see that the previous calculation predicted a value closer to the experiment for the 14% Ni sample. In Ref. 17, all calculations were performed in the same way as in the present study, but with the important difference that the c/a ratio was relaxed before the magnetic spin. In our calculation, we relax both the c/a ratio and the spin simultaneously. An example of such a calculation for the Fe<sub>66</sub>Ni<sub>14</sub>Cr<sub>20</sub> alloy can be seen in figure 6.

In figure 6, we show the c/a relaxation result of the hcp structure before the spin is optimized in black. The result is a clear double minima that correspond to the low spin solution on the left, and the high spin solution to the right. The normal way to optimize the spin from a double minima solution is to choose the lowest minima (in this case the low spin solution on the left side) and then perform a fixed spin calculation at that point along the dashed line denoted "Local minimum". If the c/a and spin optimization are done simultaneously, the final solution will be found at the point denoted "Global minimum" in the figure.

We notice that the reason for such delicate global minimum in these alloys is due to the magnetic transition seen in the hcp phase.<sup>16</sup> At larger Ni content, the high spin solution is stabilized and no similar peculiar behavior is found. The high value of the measured SFE for the Fe<sub>66</sub>Ni<sub>14</sub>Cr<sub>20</sub> alloy compared to our calculations may hence be due to a low spin state present at the stacking fault in the sample. The SFE is very sensitive to the magnetic moment at this composition as can be seen in figure 6. We hence speculate that the low spin may be due to a local fluctuation in the Cr content since Cr is the element that most strongly influences the local magnetic state in the calculation. The simulations do neglect the nitrogen and carbon contents in the alloys so there is still a possibility that the high SFE for the measured Fe<sub>66</sub>Ni<sub>14</sub>Cr<sub>20</sub> sample could be due to segregation of these elements but since we have a similar level of nitrogen and carbon in all samples we consider this possibility as unlikely. The large scatter of the measurements on sample #2 also indicate that there may be additional strain in-

Sample	Calc.	Ref. [17]	$\gamma^*$	$\gamma^\infty$
#1	16.8	14	21.5±1.9	16.9±1.9
#2	18.9	26.5	30.3±7.0	25.8±7.0
#3	25.0	26.5	26.9±3.1	22.4±3.1
#4	29.4	-	35.4±3.6	30.9±3.6
#5	26.0	20	26.1±5.3	21.6±5.3
#6	28.8	28	34.8±2.4	30.3±2.4

TABLE II: Measured and calculated SFE values for the stainless steel samples in units of mJ/m<sup>2</sup>. Also included are results from Ref. [17].

fluences from nearby defects such as dislocations or other stacking faults.

### 2. $FeNi_{(14-20)}Cr_{20}Mn_8$ samples

Previous results have shown that the addition of low amounts of Mn decreases the SFE in the Fe-Mn binary system<sup>53</sup> to a minimum at about 15 atomic % Mn,<sup>13,46,53</sup> and further increase of the Mn content above 20 atomic % clearly increases the SFE.<sup>14,54</sup> The magnitude of this effect has also been reported to depend on the Ni concentration, at least in the low Mn concentration range.<sup>17</sup> It should be pointed out that the previous results are based on Fe-Mn alloys, or Mn containing stainless steels with different compositions from the stainless steels in the present case.

In this study, the calculations always result in an increase in SFE when Mn is introduced. The effect is large and strongly dependent on Ni concentration. A minimum in this Mn effect can be seen around Ni concentrations of about 16%. The reason for the calculated SFE minimum is that a local magnetic moment of Mn develops at Ni concentrations above 15% (data not shown). The interpretation of the results is complicated by the inconclusive experimental finding that the magnitude of the SFE is independent of Mn content at Ni concentration 14%. Due to the small number of measurements of Mn containing samples, it is difficult to draw more general conclusions of the effect from Mn additions on the SFE in stainless steels from the experimental points alone. The calculated SFE of the Mn containing samples does however describe the measured points in the context of a general trend where the addition of Mn always increases the SFE for the composition ranges in this study.

## IV. CONCLUSIONS

We have shown that the combination of first principles calculations and WBDF TEM measurements is suitable for dislocation characterization and to obtain reliable SFE values in stainless steel with different compositions. For all compositions, the measured result shows the same



trend as the theoretical calculation. An exception is the  $\text{Fe}_{66}\text{Ni}_{14}\text{Cr}_{20}$  case where the calculated SFE is about 6.6 mJ/m<sup>2</sup> lower than the measurement, a likely effect of inhomogeneous composition at the length scale of the stacking fault. Ni is thus shown to have a positive effect on the SFE. The effects of Mn addition are strongly non-linear and need further study. **The axial interaction model and magnetic convergence methods that were used in our DFT calculations successfully describe the magnetic and chemical contributions to the stacking fault energies, indicating that the effects that the model neglects, such as the phonon contribution and volume expansion, are of minor importance for the alloys in this study.** The generally good agreement between theory and experiment is a result of high purity control of samples, high experimental resolution, and a state-of-the-art theoretical method. Our findings show the possibilities to use calculations for the stainless steel alloy design with

tuned stacking fault energies for controlled mechanical properties in demanding applications.

## V. ACKNOWLEDGMENTS

We received financial support from the Swedish Research Council (VR) Linköping Linnaeus Initiative LiLi-NFM (grant 2008-6572) and the Swedish Government Strategic Faculty Grant in Materials Science at Linköping University (SFO Mat-LiU/AFM). The Knut and Alice Wallenberg Foundation supported the Ultra Electron Microscopy Laboratory at Linköping University operated by the Thin Film Physics Division. Financial support from Sandvik AB is acknowledged. WL and LV acknowledge the financial support from the Swedish Research Council, the Swedish Foundation for Strategic Research, and the Chinese Scholarship Council.

- 
- <sup>1</sup> O. Grassel, L. Kruger, G. Frommeyer, L. Meyer, High strength Fe-Mn-(Al, Si) TRIP/TWIP steels development - properties - application, *Int. J. Plasticity* 16 (2000) 1391.
  - <sup>2</sup> D. Pierce, J. Jimenez, J. Bentley, D. Raabe, J. Wittig, The influence of stacking fault energy on the microstructural and strain hardening evolution of Fe-Mn-Al-Si steels during tensile deformation, *Acta Materialia* 100 (2015) 178–190.
  - <sup>3</sup> B. Qin, H. K. D. H. Bhadeshia, Plastic strain due to twinning in austenitic twip steels, *Mater. Sci. Technol* 24 (2008) 969–973.
  - <sup>4</sup> B. C. De Cooman, K. China, J. Kim, High Mn TWIP steels for automotive applications, in: M. Chiaberge (Ed.), *New Trends and Developments in Automotive System Engineering*, no. ISBN: 978-953-307-517-4, InTech, Rijeka, 2011.
  - <sup>5</sup> Q. Dai, A. Wang, X. Cheng, X. Luo, Stacking fault energy of cryogenic austenitic steels, *Chinese Physics* 11 (2002) 596.
  - <sup>6</sup> A. E. Pontini, J. D. Hermida, X-Ray diffraction measurement of the stacking fault energy reduction induced by hydrogen in an AISI 304 steel, *Scripta Materialia* 37 (1997) 1831–1837.
  - <sup>7</sup> D. Pierce, J. Bentley, J. Jimenez, J. Wittig, Stacking fault energy measurements of Fe-Mn-Al-Si austenitic twinning-induced plasticity steels, *Scripta Materialia* 66 (2012) 753.
  - <sup>8</sup> C. Bampton, I. J. and M.H. Loretto, Stacking fault energy measurements in some austenitic stainless steels, *Acta Metallurgica* 26 (1978) 39.
  - <sup>9</sup> M. Ojima, Y. Adachi, Y. Tomota, Y. Katada, Y. Kaneko, K. Kuroda, H. Saka, Weak beam TEM study on stacking fault energy of high nitrogen steels, *Steel research int.* 80 (2009) 477.
  - <sup>10</sup> X. Nie, Y. Zhou, L. Zhong, D. Wang, Alloy model for the stacking fault energy, *J. Mater. Sci. Technol.* 12 (1996) 72.
  - <sup>11</sup> M. Olsson, Thermodynamic modeling of the stacking fault energy in austenitic stainless steels, *Seconde level Degree Project, diva2:738301, urn:nbn:se:kth:diva-148660*, Stockholm, Sweden (2014).
  - <sup>12</sup> S. Curtze, V. Kuokkala, A. Oikari, J. Talonen, H. Hänninen, Thermodynamic modeling of the stacking fault energy of austenitic steels, *Acta Materialia* 59 (2011) 1068.
  - <sup>13</sup> A. Saeed-Akbari, J. Imlau, U. Prahl, W. Bleck, Derivation and variation in composition-dependent stacking fault energy maps based on subregular solution model in high-manganese steels, *Metallurgical and Materials Transactions A* 40 (2009) 3076.
  - <sup>14</sup> D. Pierce, J. Jimenez, J. Bentley, D. Raabe, C. Oskay, J. Wittig, The influence of manganese content on the stacking fault and austenite/ $\epsilon$ -martensite interfacial energies in Fe-Mn-(Al-Si) steels investigated by experiment and theory, *Acta Materialia* 68 (2014) 238–253.
  - <sup>15</sup> L. Mosecker, A. Saeed-Akbari, Nitrogen in chromium-manganese stainless steels: a review on the evaluation of stacking fault energy by computational thermodynamics, *Sci and Technol of Adv. Mater.* 14 (2013) 033001.
  - <sup>16</sup> L. Vitos, J. Nilsson, B. Johansson, Alloying effects on the stacking fault energy in austenitic stainless steels from first-principles theory, *Acta Materialia* 54 (2006) 3821.
  - <sup>17</sup> S. Lu, Q. M. Hu, B. Johansson, L. Vitos, Stacking fault energies of Mn, Co and Nb alloyed austenitic stainless steels, *Acta Materialia* 59 (2011) 5728.
  - <sup>18</sup> H. Idrissi, K. Renard, L. Ryelandt, D. Schryvers, P. J. Jaques, On the mechanism of twin formation in Fe-Mn-C TWIP steels, *Acta Materialia* 58 (2010) 2464.
  - <sup>19</sup> J. Kim, S.-J. Lee, B. C. De Cooman, Effect of al on the stacking fault energy of Fe-18Mn-0.6C twinning-induced plasticity, *Scripta Materialia* 65 (2011) 363–366.
  - <sup>20</sup> T. Balk, K. Hemker, High resolution transmission electron microscopy of dislocation core dissociations in gold and iridium, *Philosophical Magazine A* 81 (2001) 1507.
  - <sup>21</sup> D. Cockayne, I. Ray, M. Whelan, Investigations of dislocation strain fields using weak beams, *Philos. Mag.* 20 (1969) 1265.
  - <sup>22</sup> D. Cockayne, The weak-beam technique as applied to dissociation measurements, *Journal de Physique* 35 (1974) C7–141.
  - <sup>23</sup> I. Ray, D. Cockayne, The dissociation of dislocations in

- silicon, *Proc. R. Soc. Lond. A* 325 (1971) 543.
- <sup>24</sup> M. Whelan, Dislocation interactions in face-centred cubic metals, with particular reference to stainless steel, *Proc. R. Soc. Lond. Ser. A* 249 (1959) 114.
  - <sup>25</sup> R. Heidenreich, W. Shockley, *Structure of metals*, Bristol Conf. on strength of solids, p. 57. London: Physical Society (1948).
  - <sup>26</sup> A. Aerts, P. Delavignette, R. Stems, S. Amelinck, Stacking fault energy in silicon, *J. Appl. Phys.* 33 (1962) 3078.
  - <sup>27</sup> A. Teklu, H. Ledbetter, S. Kim, L. Boatner, M. McGuire, V. Keppens, Single-crystal elastic constants of Fe-15Ni-15Cr alloy, *Metall. and Mat. Trans. A* 35 (2004) 3149.
  - <sup>28</sup> D. Williams, C. B. Carter, *Transmission Electron Microscopy*, Plenum Press, New York, 1996, p. 407.
  - <sup>29</sup> L. Rémy, A. Pineau, Temperature dependence of stacking fault energy in close-packed metals and alloys, *Materials Science and Engineering* 36 (1978) 47.
  - <sup>30</sup> J. H. Jun, C. S. Choi, Variation of stacking fault energy with austenite grain size and its effect on the MS temperature of  $\gamma \rightarrow \epsilon$  martensitic transformation in Fe-Mn alloy, *Materials Science and Engineering A* 257 (1998) 353–356.
  - <sup>31</sup> H. Suzuki, *Sci. Rep. Res. Inst. Tohoku Univ. A* 4 (1952) 455.
  - <sup>32</sup> K. Ishida, Direct estimation of stacking fault energy by thermodynamic analysis, *Phys. Status Solidi (a)* 36 (1976) 717.
  - <sup>33</sup> T. Oguchi, K. Terakura, N. Hamada, Magnetism of iron above the curie temperature, *J. Phys. F* 13 (1983) 145.
  - <sup>34</sup> L. Vitos, I. Abrikosov, B. Johansson, Anisotropic lattice distortions in random alloys from first-principles theory, *Phys. Rev. Lett.* 87 (2001) 156401.
  - <sup>35</sup> P. Soven, Coherent potential model of substitutional disordered alloys, *Phys. Rev.* 156 (1967) 809.
  - <sup>36</sup> L. Vitos, P. Korzhavyi, B. Johansson, Elastic property maps of austenitic stainless steels, *Phys. Rev. Lett.* 88 (2002) 155501.
  - <sup>37</sup> L. Vitos, P. Korzhavyi, B. Johansson, Stainless steel optimization from quantum mechanical calculations, *Nat. Mater.* 2 (2003) 25.
  - <sup>38</sup> G. Grimvall, Polymorphism of metals. iii. theory of the temperature-pressure phase diagram of iron, *Phys. Scr.* 13 (1976) 59.
  - <sup>39</sup> F. J. Pinski, J. Staunton, B. L. Györfy, D. Johnson, G. M. Stocks, Ferromagnetism versus antiferromagnetism in face-centered-cubic iron, *Phys. Rev. Lett.* 56 (1986) 2096.
  - <sup>40</sup> B. L. Györfy, A. Pindor, G. M. Stocks, J. Staunton, H. Winter, A first-principles theory of ferromagnetic phase transitions in metals, *J. Phys. F* 15 (1985) 1337.
  - <sup>41</sup> G. Grimvall, Spin disorder in paramagnetic fcc iron, *Phys. Rev. B* 39 (1989) 12300.
  - <sup>42</sup> M. Shimizu, Effects of spin fluctuations in itinerant electron ferromagnets, *Physics Letters A* 81 (1981) 87–90.
  - <sup>43</sup> L. Vitos, P. Korzhavyi, B. Johansson, Evidence of large magnetostructural effects in austenitic stainless steels, *Phys. Rev. Lett.* 96 (2006) 117210.
  - <sup>44</sup> J. P. Perdew, K. Burke, M. Ernzerhof, Generalized gradient approximation made simple, *Phys. Rev. Lett.* 77 (1996) 3865–3868.
  - <sup>45</sup> T. Lee, H. Ha, B. Hwang, S. Kim, E. Shin, Effect of carbon fraction on stacking fault energy of austenitic stainless steels, *Metall. Mater. Trans. A* 43 (2012) 4455–4459.
  - <sup>46</sup> R. E. Schramm, R. P. Reed, Stacking fault energies of seven commercial austenitic stainless steels, *Metallurgical and Materials Transactions A* 6 (1975) 1345.
  - <sup>47</sup> P. Brofman, G. Ansell, On the effect of carbon on the stacking fault energy of austenitic stainless steels, *Metall. Mater. Trans. A* 9 (1978) 879–880.
  - <sup>48</sup> D. Gerthsen, C. Carter, Stacking-fault energies of GaAs, *Phys. Stat. sol. (a)* 136 (1993) 29.
  - <sup>49</sup> M. Luysberg, D. Gerthsen, On the dissociation of dislocations in InP, *Phys. Stat. sol. (a)* 146 (1994) 157.
  - <sup>50</sup> J. W. Brooks, M. H. Loretto, R. E. Smallman, In situ observations of the formation of martensite in stainless steel, *Acta Metallurgica* 27 (1979) 1829.
  - <sup>51</sup> J. W. Brooks, M. H. Loretto, R. E. Smallman, Direct observations of martensite nuclei in stainless steel, *Acta Metallurgica* 27 (1979) 1839.
  - <sup>52</sup> P. J. Ferreira, P. Müllner, A thermodynamic model for the stacking-fault energy, *Acta Mater.* 46 (1998) 4479.
  - <sup>53</sup> Y. K. Lee, C. S. Choi, Driving force for  $\gamma - \epsilon$  martensitic transformation and stacking fault energy of  $\gamma$  in Fe-Mn binary system, *Metallurgical and Materials Transactions A* 31 (2000) 355.
  - <sup>54</sup> E. Mazancová, K. Mazanec, Stacking fault energy in high manganese alloys, *Materials Engineering* 16 (2009) 26.